MAPPING A SINGLE CELL TRACTION FIELD WITHIN A 3D COLLAGEN EXRACELLULAR MATRIX USING A FLUORESCENCE MICROSCOPE

A Thesis

Presented to the Faculty of the Graduate School

of

Cornell University

In Partial Fulfillment of the Requirements for the Degree of

Master of Science

by

Matthew Steven Hall

August 2012

ABSTRACT

Three dimensional (3D) cell culture is becoming mainstream as it is recognized that many animal cell types require the biophysical and biochemical cues within the extracellular matrix (ECM) to perform truly physiologically realistic functions. However, tools for characterizing cellular mechanical environment are largely limited to cells cultured on a 2D substrate. We present a three dimensional (3D) traction microscopy that is capable of mapping 3D stress and strain within a soft and transparent ECM using a fluorescence microscope and a simple forward data analysis algorithm. We validated this technique by mapping the strain and stress field within the bulk of a thin polyacrylamide gel layer indented by a millimeter size glass ball, together with a finite element analysis. The experimentally measured stress and strain fields are in excellent agreements with results of the finite element simulation. The unique contributions of the presented 3D traction microscopy method are: (a) the use of a fluorescence microscope in contrast with the confocal microscope that is required for the current 3D traction microscopy in the literature; (b) the determination of the pressure field of an incompressible gel from strains; (c) the simple forward data analysis algorithm compatible with a nonlinear ECM. We apply our 3D traction microscopy method to map the 3D stress field over time around an MDA-MB-231 malignant epithelial breast cancer cell migrating through a type I collagen ECM. Both the normal and shear components of the resulting 3D stress field are in agreement with molecular and cellular scale processes involved in cell motility. Future application of our method, including detecting cancer cell malignancy and understanding the mechanics of each step of a cell's journey during cancer metastasis are discussed.

BIOGRAPHICAL SKETCH

Matthew Hall is currently a graduate student in the Department of Biological and Environmental Engineering at Cornell University. For his Master of Science degree Matthew declared a major area in Biological Engineering and a minor area in Mechanics of Materials. Previously, Matthew attended Cornell University from August 2006 – May 2010 receiving a Bachelor of Science in Biological Engineering in January 2010 and a Master of Engineering in Biomedical Engineering in May 2010. Before coming to Cornell, Matthew attended Downingtown East High School in his hometown of Exton, Pennsylvania. After successful completion of the Master of Science degree Matthew plans to continue his current research at Cornell in pursuit of a Doctor of Philosophy in Biological Engineering.

ACKNOWLEDGMENTS

Chapter 1 consists of a paper for which I am a first author “Mapping 3D Stress and Strain Fields within a Soft Hydrogel using a Fluorescence Microscope” accepted for publication and currently in press at Biophysical Journal. The paper is reproduced with permission of the publisher Cell Press an imprint of Elsevier B.V. I acknowledge the contribution of my co-authors Rong Long, Chung-Yuen Hui, and Mingming Wu. In particular I acknowledge the contribution of my co-first-authored Rong Long who performed the theoretical and numerical component of the work. In addition, Mingming Wu and I would like to thank Cynthia Reinhart-King, Joseph Califano, and Yu-li Wang for helpful discussions on polyacrylamide gel preparation and the microsphere indentation method.

Chapter 2 consists of a yet to be published paper for which I am a first author titled “Mapping a Single Cell Traction Field within a 3D Extracellular Matrix using a Fluorescence Microscope”. I acknowledge the contributions of my co-authors Xinzeng Feng, Rong Long, Chris Roh, Beum Jun Kim, Chung-Yuen Hui, and Mingming Wu. In particular I would like to acknowledge the contribution of Xinzeng Feng who performed the numerical component of the work.

My coauthors and I acknowledge funding for the papers in chapters 1 and 2.

Mingming Wu, Xinzeng Feng , Rong Long, and I thank support from the National Center for Research Resources (5R21RR025801-03) and the National Institute of General Medical Sciences (8 R21 GM103388-03) of the National Institutes of Health. Rong Long acknowledge support from Materials and Surface Engineering program, CMMI, National Science Foundation (grant no. CMMI-0900586). Chung-Yuen Hui

acknowledges the support of the US department of energy, Office of Basic Energy Science, Division of Material Sciences and Engineering under award DE-FG02-07ER46463.

TABLE OF CONTENTS

LIST OF FIGURES

LIST OF TABLES

CHAPTER 1

3D TRACTION MICROSCOPY METHOD AND VALIDATION

1.1. **Introduction**

Biomechanical cues from the extracellular matrix (ECM), such as adhesion and compliance, play important roles in functions of most animal cell types [1, 2]. When plated on a 2D substrate, cells grow [3], differentiate [4], and migrate [5-7] differently based on the substrate compliance and the adhesiveness. Substrate compliance influences adhesion structures and dynamics [6], cytoskeleton assembly and cell spreading [8, 9]. A notable example is that human mesenchymal stem cells are found to differentiate into cells that exhibit neurogenic, myogenic and osteogenic phenotypes when plated on polyacrylamide gel substrates with soft, stiffer and very stiff matrices respectively [4].

In vivo, most animal cells reside in a 3D ECM, and require the biophysical and biochemical cues from the ECM to perform truly physiologically relevant cellular functions [10-13]. Indeed, cells are found to exhibit smaller focal adhesion complexes, downgrade integrin expressions in 3D ECM in comparison to their counterparts in 2D [14]. As a result, an increasing number of *in vitro* models culture cells within the bulk of 3D hydrogels, instead of the traditional 2D substrates [10, 11, 15, 16]. However, current tools for characterizing stress and strain fields within a soft biomaterial, such as traction microscopy, are largely limited to 2D [17-19]. There is a need for developing tools for quantifying 3D strain and stress fields within a 3D ECM.

The current 3D traction microscopy that is designed to map the stress and strain field in 3D ECM is still in its infant stage [20-22]. This is, in part, due to the requirement of a confocal microscope that is often not available in the labs of individual investigators; and in part, due to the complex data analysis algorithm ensued. Maskarinec et al. measured the 3D displacement, strain and stress field within a thin layer of polyacrylaimde gel deformed by a single fibroblast cell cultured on the gel surface [20, 23]. They used confocal microscopy to image the micrometer size fluorescent beads embedded in the gel and determined the displacement fields using a digital volume correlation method (DVC) [24]. Concurrently, Hur et al. developed a different method to measure the 3D stress and strain field within a polyacrylamide gel deformed by a single endothelial cell, cultured on the gel surface [21]. They also used confocal microscopy to image fluorescent beads embedded in the gel. Bead positions were determined by finding the maximum intensity of the bright spots, and displacements were determined using the nearest neighbor and a bead pattern recognition algorithm. The bead displacements were then used as boundary conditions to solve the 3D governing equations of linear elasticity through finite element analysis. Both of these works clearly demonstrated that cells exert 3D tractions even when cultured on 2D substrates. More recently, Legant et al. quantified cellular tractions of a single cell cultured within a synthetic elastic hydrogel. They used embedded fluorescent beads in conjunction with a confocal microscope for measuring bead displacements due to cellular tractions [22]. The cell surface was reconstructed from confocal microscopy and was discretized into small elements. Finite element calculations were then performed to obtain the discretized Green's functions on these surface elements. An

ill posed inverse problem was then solved using optimization method to determine the cell tractions from the bead displacements. This method provided high spatial resolution 3D traction field at the cell surface, but required that the gel is linearly elastic, isotropic and homogeneous, an inherent limitation when using the superposition of Green's functions. In addition, this technique needs a large volume of image data acquisition and complex data processing.

Motivated by the need to map the stress and strain field around a single cell for studies of cell-ECM interactions, we developed a 3D traction microscopy that allows for the mapping of the strain and stress field within a soft and transparent hydrogel using a fluorescence microscope and a simple-to-implement forward data analysis algorithm. This technique takes advantage of a recently developed 3D defocused particle tracking method [25] for bead displacement measurements; and a moving least square interpolation method (MLSIM) for the computation of the strain field from the bead displacements [26]. As a result, it allows for the use of a fluorescence instead of confocal microscope, and improves the temporal resolution of the current 3D traction microscope from a few minutes to a few seconds. Furthermore, this technique is not limited to the linear elastic gel, can be readily modified to study cellular traction within biological gels (often display nonlinear elasticity [27]) such as collagen.

1.2. Materials and methods

1.2.1 Binding a Polyacrylamide gel to an activated cover slide

Glass coverslips of two different sizes were used in this procedure. One side of a smaller glass coverslip (No 1, 45mm x 50mm, Thermo Scientific, Waltham, MA) was

treated with RAINEX to make it hydrophobic. The surface of a larger glass coverslip (No 1, 48mm x 65mm, Thermo Scientific, Waltham, MA) was activated to covalently bond to a polyacrylamide gel sheet using methods adapted from the protocol of Reinhart-King et al. [28]. First, a cotton swab was used to evenly coat the surface with 0.1N NaOH and the coverslip was air dried. Second, a Pasteur pipette was used to coat the surface with 60ul of 3-aminopropyltrimethoxysilane (APTMS, Aldrich, St. Louis, MO). After incubating 5 minutes the coverslip was washed with distilled water and air dried. Third, the coverslip was coated with 2ml of 0.5% gluteraldehyde (Aldrich, 70%) in PBS and incubated for 30 minutes. Last, the coverslip was washed in distilled water and air dried completing the surface activation.

A polyacrylamide solution with a final concentration of 3% acrylamide (Bio-Rad, Hercules CA, 40% w/v), 0.1% N, N-methylene-bis-acrylamide (BIS, Bio-Rad, 2% w/v), 300 mM HEPES (EMD Chemicals, Gibbstown, NJ), 0.05% Tetramethylethylenediamine (TEMED, Sigma, St. Louis, MO) and 0.83um green fluorescent microspheres (Cat. No. G830, Thermo Scientific) was prepared. The solution was adjusted to a pH of 6 with Hydrochloric Acid and then degassed. Molecular biology grade ethyl alcohol was added to achieve a final concentration of 7%. Ammonium Persulfate (Aldrich) was added to achieve a final concentration of 0.05% w/v to initiate polymerization. The Polyacrylamide solution was pipetted onto the hydrophobic side of the smaller coverslip. The activated side of the larger coverslip was lowered into contact with the polyacrylamide solution until the solution covered the entire area of the smaller coverslip. The polyacrylamide layer and smaller coverslip were suspended upside down from the larger coverslip to polymerize for 2

hours in a 100% humidity environment. The smaller coverslip was removed and the polyacrylamide gels were immersed in distilled water for at least one day to ensure complete hydration before use.

1.2.2. Indentation method

We used the weight of a millimeter-scale glass sphere to deform a thin polyacrylamide gel layer (Figure 1.1). This method, known as the indentation method, was pioneered by Wang *et al* for determining the Young's modulus of soft gel [18]. A spherical glass ball with specific density of 2.5 g/ml and diameter of 1.17mm was used. The indentation force, equal to the weight minus the buoyancy force of the glass sphere, was 12.4 μN. For each indentation experiment, a pipette was used to place the glass sphere on the surface of the polyacrylamide gel covered by water submerging both the gel and the sphere. The sphere was then brought to the center of the image using the x-y translation stage of the microscope (Olympus IX51) and the bright field microscopy. The microscope was then switched to epi-fluorescent mode. An image of the fluorescent beads embedded within the gel was captured with the 20X objective (Olympus NA 0.4). A pipette was then used to push the glass indenter off the gel with a gentle jet of water without disturbing the gel or microscope stage. The gel returned to its un-deformed state, and a second image of the fluorescent beads was captured with the 20x objective without adjusting the stage location. We defined the center of the coordinate (0,0,0) to be at the contact point of the un-deformed sphere - gel interface (Figure 1.1) and used it as a reference point for all data taking. The gel thickness was determined by measuring the locations of the highest and lowest

fluorescent beads in the gel using the manual z-translation stage [29], which was h=134± 2.3 μm. This procedure was repeated at 10 different locations on the surface of the gel using the same sphere.

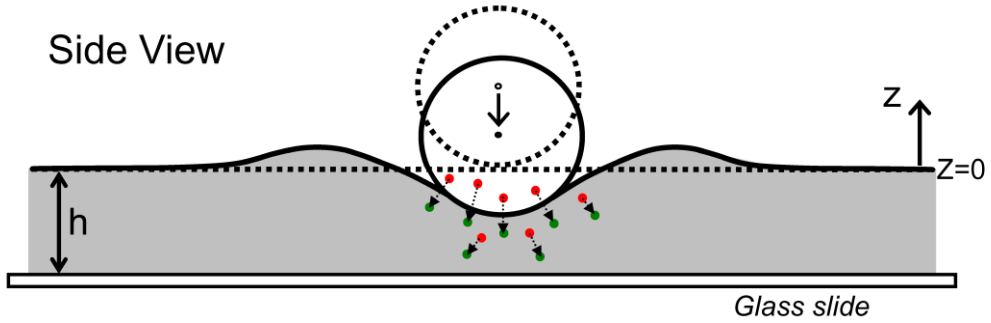

Figure 1.1 The microsphere indentation method. Schematics of a microsphere indenting on a thin polyacrylamide gel substrate. The contact point of the sphere with the un-deformed gel is defined as the origin or (0,0,0) coordinates of the system with z-axis being in the vertical direction. Fluorescent beads embedded in the gel are displaced from their original positions (red dots) to their final positions (green dots) upon the indentation of the microsphere

1.2.3. A 3D defocused particle tracking method

A defocused particle tracking method was used to measure the 3D positions of the fluorescent beads embedded within the gel [25] (Figure 1.1). The basic idea behind the defocused particle tracking method is shown in Figure 1.2A. When a point light source is positioned at the focal plane, the light converges to a point in the image plane. When the point light source is a distance z_{fo} from the focal plane, the light converges into a circular ring of diameter d in the image plane due to spherical aberration in the microscope objective lens (Figure 1.2A). In our microscope system, the defocused ring is only observed when the point light source is positioned between

the focal plane and the lens plane. The ring image can then be used to compute the (x,y,z) coordinates of the point light source.

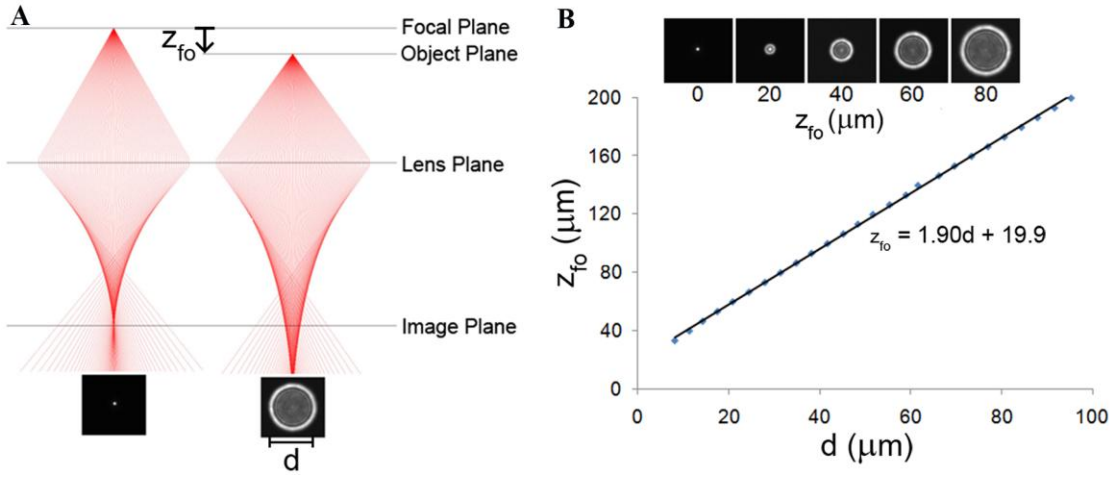

Figure 1.2 The 3D defocused particle tracking method. A: A ray tracing diagram of light traveling through a spherical lens. A point source of light in the focal plane emits rays that are bent by the lens and converge to a point at the image plane (left-side). If the point source is displaced a distance z_{fo} from the focal plane, its rays do not converge and they produce a defocused ring on the image plane with diameter d (right-side) due to spherical aberration. Representative images of a point source under each condition are inserted (bottom). Experimentally derived calibration curve of fluorescent bead z_{fo} vs defocused ring diameter d. Images of defocused rings at different z_{fo} are inserted (top).

To compute the z position of the fluorescent bead using the ring diameter, we carried out a calibration for our optical system. We measured the distance from the focal plane, $z_{fo,}$ as a function of the ring diameter d. Figure 1.2B shows that z_{fo} was linearly related to d over the z_{fo} range of (30-200μm) for the 20X objective lens (Figure 1.2B). To obtain this calibration curve, we first brought a 0.83 μm green fluorescent microsphere (Cat. No. G830, Thermo Scientific) into focus. The objective lens was then brought closer to the fluorescent bead in the z direction in 5 μm increments and an image was taken at each increment. The diameter of the ring in each image was measured using the image analysis software detailed below. It should

be noted that the lens was displaced along the z-direction during the calibration procedure, while the experimental measurements were made relative to the focal plane. In our system, displacement of the lens is not equal to displacement of the focal plane because of refractive index mismatches at the air-glass and glass-water interfaces. To account for this difference, a calibration was performed using a known spacing (an equivalent of a z-ruler) submerged in water [29]. The calibration showed that the displacement of the focal plane was 1.31 times the displacement of the lens. The experimentally derived optical correction factor 1.31 is comparable to the correction factor computed from Gaussian Optics of 1.33 where the objective lens is treated as a thin lens, the cover slide is negligibly thin, and the paraxial approximation applies. A separate calibration experiment was performed to ensure the same z_{fo} vs. d relationship applies to fluorescent beads at all locations throughout the gel. The slope of the z_{fo} vs. d linear fit was found to vary by less than 2% between beads at the top and bottom of the gel.

1.2.4. Image analysis

The (x,y,z) coordinates of the fluorescent beads were obtained from the ring image shown in Figure 1.3A using an in house MATLAB program. For each ring, the user first provided an approximation for the center and diameter of the ring through a graphical user interface by clicking at 3 points on the circumference of the ring. A search algorithm was then used to find the exact center and diameter of the ring with spatial resolution of 1 pixel. The (x,y) coordinates of the fluorescent bead were

determined using the center position of the ring, and the z coordinate of the bead was determined using the ring diameter and the calibration curve shown in Figure 1.2B.

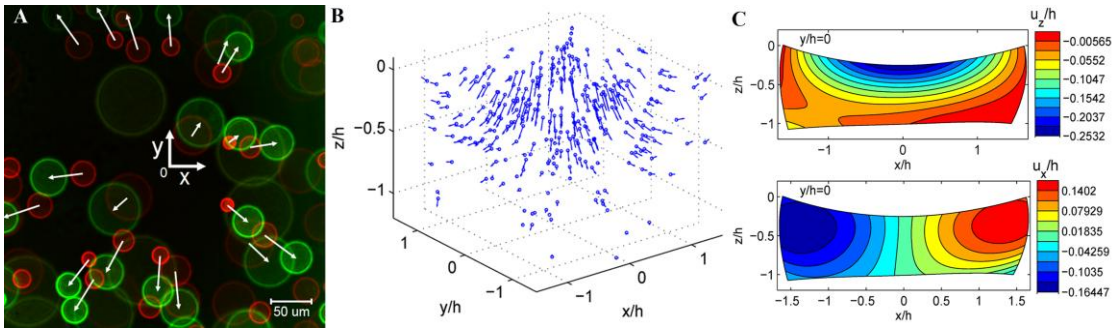

Figure 1.3 Displacement field in the indented gel. A: Combined images of fluorescent beads embedded in the un-deformed and deformed polyacrylamide gel. The red defocused rings indicate the original bead position in un-deformed gel and green rings indicate positions of fluorescent beads within the deformed gel. White arrows are drawn to indicate the xy displacement of each bead in x-y plane upon indentation. Increase in ring size indicates displacement in the negative z direction. B: Experimentally measured 3D bead displacements. The lengths of the arrows are scaled by a factor of 0.7 for better illustration. Circles indicate the initial position of beads; ends of the arrows indicate the final positions of the beads after the gel is indented. C: Continuous displacement field of u_z/h and u_x/h at cross-section y=0 (side view). The displacement fields are derived from the discrete displacements shown in (B) using MLSIM.

The fluorescent bead displacements were obtained by tracking the bead positions of the two images taken before and after the gel deformation (Figure 1.3A). To increase the spatial resolution of the bead displacements, results from 10 separate indentations with the same spherical indenter were combined into one dataset. It should be noted that it is important that the contact point between the indenter and the un-deformed gel be used as the (0,0,0) coordinates for all the measurements. The combined bead displacements were shown in Figure 1.3B.

1.2.5. Moving Least Square (MLS) Method

The bead displacement data obtained from defocused particle tracking provides a discrete measurement of displacement fields within the soft gel. Since the strains are spatial derivatives of displacements and evaluating them requires a continuous description of the displacement fields. The basic idea here is to construct a continuously differentiable displacement field from these discrete data using interpolation. Our interpolation scheme draws an idea from the mesh-free method [26]in computational mechanics, developed as an alternative to finite element method. This method uses the Moving Least Square (MLS) interpolation technique[30-32]. An advantage of the MLS method is that the interpolated field can have *continuous derivative of any order*, thus ensuring a smooth strain field. Following Belytschko et al.[26], we first construct an interpolation function $g(\mathbf{x})$ as follows:

$$g(\mathbf{x}) = \mathbf{P}^T(\mathbf{x})\mathbf{a}(\mathbf{x}), \tag{1}$$

where $\mathbf{x}$ represents the Cartesian coordinates (x,y,z) of a point in the undeformed configuration ($\mathbf{x}^T = [x, y, z]$; the superscript T denotes transpose). $\mathbf{P}^{\mathrm{T}}(\mathbf{x})$ is a polynomial basis and $\mathbf{a}(\mathbf{x}) = [a_0(\mathbf{x}), a_1(\mathbf{x}), a_2(\mathbf{x}), ...]$ can be regarded as unknown coefficients for this basis. Note that $a_i(\mathbf{x})$ are scalar functions of position. For example, if a linear basis is used, $\mathbf{P}^{\mathrm{T}}(\mathbf{x})$ and $g(\mathbf{x})$ are:

$$\mathbf{P}^T(\mathbf{x}) = [1, x, y, z], \qquad g(\mathbf{x}) = a_0(\mathbf{x}) + a_1(\mathbf{x})x + a_2(\mathbf{x})y + a_3(\mathbf{x})z. \tag{2a,b}$$

We adopt a cubic basis in our data processing, i.e.,

$$\mathbf{P}^T(\mathbf{x}) = [1,\ x,\ y,\ z,\ x^2,\ y^2,\ z^2,\ xy,\ xz,\ yz,\ x^3,\ y^3,\ z^3, \ldots \\ x^2y,\ x^2z,\ y^2x,\ y^2z,\ z^2x,\ z^2y,\ xyz]. \tag{2c}$$

It is important to note that **a**(**x**) depends on **x**, otherwise g(**x**) reduces to a regular polynomial function. Suppose in the undeformed gel there are n beads located at $\mathbf{b}_I$ ($I=1,\ldots,n$) where $\mathbf{b}_I^T = \left[b_{Ix}, b_{Iy}, b_{Iz} \right]$. Let w_I denote a physical quantity associated with bead I, (e.g. the x-component of the displacement of the I^{th} bead). To determine the coefficient functions **a**(**x**), we perform a weighted least square fitting at every point **x** that minimizes the following norm:

$$L = \sum_{I=1}^{n} f(\mathbf{x} - \boldsymbol{b}_I) \left[\boldsymbol{P}^T(\boldsymbol{b}_I)\boldsymbol{a}(\boldsymbol{b}_I) - w_I \right]^2 \tag{3}$$

and $f(\mathbf{x}-\mathbf{b}_I)$ is a weight function that decays with $\left|\boldsymbol{x} - \boldsymbol{b}_I\right|$, that is, the weight decreases as the point of interest moves away from bead I. As a result, the coefficients **a**(**x**) varies from point to point and is determined mostly by the displacements of beads within a neighborhood of **x**. We used the following exponentially decaying weight function proposed by Belytschko *et. al* [26],

$$f(\mathbf{x}-\mathbf{b}_I) = \begin{cases} \dfrac{\exp(1-d^2/d_m^2)-1}{e-1} & d \le d_m \\ 0 & d > d_m \end{cases}, \quad d = \left|\mathbf{x}-\mathbf{b}_I\right|. \tag{4}$$

In eq. (4), d_m is a cut-off distance and is chosen to be

$$d_m = 2\sum_{I=1}^{m} \left|\mathbf{x}-\mathbf{b}_I\right| / m, \tag{5}$$

where m is an adjustable parameter that is smaller than n, the total bead number. This parameter determines the decaying length of the weight function f and thus controls the quality of the fitted results. For example, if m is too small, only a few bead data points are included in the MLS fitting, which can cause severe non-smoothness in the

fitted fields. As *m* increases towards the total bead number *n*, the fitted field becomes smoother but should converge at a large enough *m*. This is because the newly added data points by further increasing *m* contribute little to the MLS fitting due to the exponential decaying behavior of the weight function. We have verified in our indentation data that the fitted strain fields are insensitive to *m* for *m*=180 and *m*=285 (total bead number is 285). We chose *m* = 180 to save computation time while achieving sufficient accuracy.

To determine the unknown vector function **a**(**x**), we minimize the least square error norm *L* in eq. (3). This procedure leads to a set of linear equations for the vector function **a**(**x**), which can be solved exactly. The interpolation function is found to be

$$g(\mathbf{x}) = \mathbf{P}^T(\mathbf{x})\mathbf{a}(\mathbf{x}) = \mathbf{P}^T(\mathbf{x})\mathbf{A}^{-1}(\mathbf{x})\mathbf{B}(\mathbf{x})\mathbf{w}, \tag{6}$$

where

$$\mathbf{A}(\mathbf{x}) = \sum_{I=1}^{n} f(\mathbf{x}-\mathbf{b}_I)\mathbf{P}(\mathbf{b}_I)\mathbf{P}^T(\mathbf{b}_I), \tag{7a}$$

$$\mathbf{B}(\mathbf{x}) = \left[f(\mathbf{x}-\mathbf{b}_1)\mathbf{P}(\mathbf{b}_1), ..., f(\mathbf{x}-\mathbf{b}_n)\mathbf{P}(\mathbf{b}_n) \right], \tag{7b}$$

$$\mathbf{w}^T = [w_1,\ w_2,\ ...,\ w_n]. \tag{7c}$$

Applying the interpolation function in eq. (6) to each of the three displacement components, we obtain a continuously differentiable 3D displacement field within the gel.

1.2.6. Computing strain and stress fields

The strain fields can be determined by calculating the spatial derivatives of the

displacements. For simplicity, we use linear elasticity formulation where the strain tensor is given by

$$\boldsymbol{\varepsilon} = \left(\nabla \mathbf{u} + \left(\nabla \mathbf{u}\right)^T\right)/2, \quad \text{or} \quad \varepsilon_{ij} = \frac{1}{2}\left(\frac{\partial u_i}{\partial x_j} + \frac{\partial u_j}{\partial x_i}\right), \tag{8}$$

where **u** is the displacement vector: $\mathbf{u}^T = [u_x,\ u_y,\ u_z]$. The subscripts *i* and *j* can be 1, 2 or 3, referring to the Cartesian coordinates *x*, *y* and *z* respectively. Eq. (8) allows us to compute the strain from the interpolated displacement field using the derivatives of the interpolation function:

$$\frac{\partial g}{\partial x_i} = \left[\frac{\partial \mathbf{P}^T}{\partial x_i}\mathbf{A}^{-1}\mathbf{B} - \mathbf{P}^T\mathbf{A}^{-1}\frac{\partial \mathbf{A}}{\partial x_i}\mathbf{A}^{-1}\mathbf{B} + \mathbf{P}^T\mathbf{A}^{-1}\frac{\partial \mathbf{B}}{\partial x_i}\right]\mathbf{w}. \tag{9}$$

Once the strain field is determined, we can use the constitutive relations to obtain the stress field. Assuming the material is isotropic and homogeneous, the stress field is given by the Hooke's law in linear elasticity, i.e. ,

$$\sigma_{ij} = \lambda\varepsilon_b\delta_{ij} + 2\mu\varepsilon_{ij}, \qquad \lambda = 2\nu\mu/\left(1-2\nu\right), \tag{10}$$

Where $\varepsilon_b = \varepsilon_{xx} + \varepsilon_{yy} + \varepsilon_{zz}$ is the bulk strain, μ is the shear modulus and ν is the Poisson's ratio.

A difficulty arises when the gel is incompressible or close to incompressible, that is, when ν~0.5 (or $\lambda \to \infty$). In this case the bulk strain ε_b is close to zero so it is very difficult to numerically evaluate the product $\lambda\varepsilon_b$. As a result, the normal stress components (e.g. σ_{zz}) cannot be directly determined from the strain field. Since the short time mechanical behavior of most gels is close to incompressible, the determination of the full stress tensor from the strains is a non-trivial problem that

needs to be addressed. For an incompressible material, $\lambda\varepsilon_b$ is the average of the three normal stress components and is usually denoted by -*p*, where *p* is often interpreted as a hydrostatic pressure [33]. It should be noted that the $\lambda\varepsilon_b$ term in (10) is taken to be zero for incompressible materials in previous works [20, 23]. Since an incompressible material can support hydrostatic stress without deformation, the assumption of $\lambda\varepsilon_b = 0$ may lead to substantial error in the calculation of stresses in the gel. To illustrate this point, we consider a simple example where a concentrated compressive normal force acts on the surface of an incompressible linear elastic half space. An exact solution for the stress field has been obtained, known as the Boussinesq solution and can be found in Johnson [34]. Using this solution, one can easily show that setting $\lambda\varepsilon_b = 0$ in eq. (10) makes at least 33% relative error for all three normal stress components.

We propose the following solution to resolve this problem. As mentioned earlier, for incompressible solids, the $\lambda\varepsilon_b$ term in eq. (10) should be replaced by an undetermined pressure term –*p* [33], i.e.,

$$\sigma_{ij} = -p\delta_{ij} + 2\mu\varepsilon_{ij}. \tag{11}$$

where δ_{ij} is the Kronecker delta defined by $\delta_{ij} = 0$ if $i \neq j$ and $\delta_{ij} = 1$ otherwise. The stresses must satisfy the following equilibrium equations under static or quasi-static conditions:

$$\sum_{j=1}^{3} \frac{\partial \sigma_{ij}}{\partial x_j} = 0. \tag{12}$$

Substituting (11) into (12), we obtain

$$\frac{\partial p}{\partial x_i} = \mu \nabla^2 u_i + \mu \frac{\partial \varepsilon_b}{\partial x_i} \quad . \tag{13}$$

Integrating eq. (13) gives the

$$p(\mathbf{x}) - p(\mathbf{x}_0) = \mu \int_{\mathbf{x}_0}^{\mathbf{x}} \left(\nabla^2 \mathbf{u} \right) \bullet d\mathbf{s} + \mu \left[\varepsilon_b(\mathbf{x}) - \varepsilon_b(\mathbf{x}_0) \right]. \tag{14}$$

The first integral in (14) can be evaluated along any path joining $\mathbf{x}_0$ to $\mathbf{x}$. Usually one can choose $\mathbf{x}_0$ so that $p(\mathbf{x}_0)$ is known, e.g., $\mathbf{x}_0$ can be a point where all the stress components vanish (e.g. far away from our region of interest) or a point where one of the normal stress components is known. In principle, ε_b=0 is valid for incompressible materials at any spatial locations; we retain the bulk strain term in (13) since it may not be exactly zero in experiments. For compressible solids, the equations above are also valid but may not be very useful in this case since the stresses can be directly determined from strains. The term $\nabla^2 \mathbf{u}$ in eq. (14) is obtained by taking the Laplacian of the interpolation function in eq. (6), which is found to be

$$\begin{aligned} \nabla^2 g = \Big[& \left(\nabla^2 \mathbf{P}^T \right) \mathbf{A}^{-1} \mathbf{B} - \mathbf{P}^T \mathbf{A}^{-1} \left(\nabla^2 \mathbf{A} \right) \mathbf{A}^{-1} \mathbf{B} + \mathbf{P}^T \mathbf{A}^{-1} \left(\nabla^2 \mathbf{B} \right) \\ & + \sum_{i=1}^{3} 2 \frac{\partial \mathbf{P}^T}{\partial x_i} \left(-\mathbf{A}^{-1} \frac{\partial \mathbf{A}}{\partial x_i} \mathbf{A}^{-1} \mathbf{B} + \mathbf{A}^{-1} \frac{\partial \mathbf{B}}{\partial x_i} \right) \\ & + \sum_{i=1}^{3} 2 \mathbf{P}^T \left(\mathbf{A}^{-1} \frac{\partial \mathbf{A}}{\partial x_i} \mathbf{A}^{-1} \frac{\partial \mathbf{A}}{\partial x_i} \mathbf{A}^{-1} \mathbf{B} - \mathbf{A}^{-1} \frac{\partial \mathbf{A}}{\partial x_i} \mathbf{A}^{-1} \frac{\partial \mathbf{B}}{\partial x_i} \right) \Big] \mathbf{w} \end{aligned} \quad . \tag{15}$$

The pressure field is determined by (14) where we evaluate $\nabla^2 \mathbf{u}$ by applying (15) to each of the three displacement components $u_{i,}$. Once the pressure field is obtained, the stress filed can be easily calculated using (11).

1.2.7. Finite Element Analysis

In our early work and others, it has been found that the gel deformation depends sensitively on gel thickness *h* [28, 29]. More specifically, the gel deformation is found to depend on two parameters, *R/h* and δ / h, where R is the radius of the indenter and δ is the indentation depth at the contact point (See text and supplementary material of [29]). We thus chose values of *R/h*=4.366 and $\delta / h = 0.2532$ to be exactly the same as in experiments for the finite element method (FEM) calculation. Note that, in experiments, we have ball radius *R* =585 μm, the gel layer thickness *h* = 134μm and the indentation depth δ = 33.93 μm. Briefly, the deformation of the gel layer is simulated using a commercial finite element software, ABAQUS (Version 6.7, Dassault Systemes Corp., Providence, RI). Axisymmetry of the indentation setup allows us to use axisymmetric elements to simulate gel deformation.. The gel layer was modeled as a circular disk with thickness *h* and radius 20*h* made of incompressible neo-Hookean solid, which is the simplest hyper-elastic material model for elastomers and was derived based on the Gaussian statistics of polymer chains[35]. The indenter was modeled as a rigid sphere of radius *R* and the indenter-gel interface was assumed to in frictionless condition. The gel layer was discretized into 25,547 linear quadrilateral axisymmetric elements (CAX4RH) biased towards the center of contact region, where the element size is about 0.0167*h*. Hybrid elements were used where the hydrostatic pressure field due to incompressibility was independently interpolated and was solved together with the displacement field through the finite element equations.

1.3. Results and discussions

1.3.1. Discrete and continuous displacement fields in the gel

The discrete displacements of the embedded fluorescent beads upon the deformation of the gel were obtained using the 3D defocused particle tracking method. A 3D plot of the bead positions and bead displacements are shown in Figure 1.3B. A total of 285 fluorescent beads were tracked in this data set. Depending on the location of a bead, magnitudes of the measured bead displacement ranges from 0.5 μm to 35 μm, demonstrating the highly non-uniform deformation field within the gel.

We first computed the continuous and differentiable displacement field using the discrete bead displacements, which was a necessary step for computing the 3D strain field. Using the MLSIM introduced above, we transformed the discrete bead displacements shown in Figure 1.3B into a continuous displacement field (Figure 1.3C). The characteristic deformation field due to an indenter is distinctly shown in Figure 1.3C. For clear presentation, we took advantage of axisymmetry of the deformation field and choose to render the displacement field on the cross section of *y=0*. The contours of displacement components u_x and u_z at the cross section of y=0 are shown in Fig. 3C. The displacement component u_y is negligible in this plane, as expected from axisymmetry of the deformation field. Figure 1.3C shows that the absolute values of u_x and u_z are symmetric with respect to the x=0 plane. Therefore, in the following discussion we only present results in the plane y=0 and x>0 as shown in Fig. 4.

1.3.2. Experimentally obtained 3D strain field

We compute the strain fields using eq. (8) and (9) from the continuously differentiable displacement field shown in Fig. 3C or Fig. 4 (A, C). The results are plotted in Figure 1.5 for the three normal strain components: ε_{xx}, ε_{yy}, ε_{zz}. Because of the axisymmetry, ε_{xz} is the only non-vanishing shear strain component on the *y=0* plane out of the three: ε_{xy}, ε_{yz}, ε_{xz}. Eq. (10) indicates that ε_{xz} is proportional to the shear stress σ_{xz} by a coefficient of 2μ. As a result, the ε_{xz} component is not included in Figure 1.5 since it has a similar distribution as σ_{xz} which will be presented in Figure 1.6.

As mentioned earlier, at a time scale much shorter than the characteristic diffusion time, gels behave as incompressible materials due to negligible amount of solvent migration. This is the case for our indentation experiment, as the experimental time scale is about several minutes and the diffusion time scale is on the order of hours [29]. Therefore, we set the Poisson's ratio for the polyacrylamide gel in our experiment to be 0.5, which is consistent with the compression test result in Maskarinec et al. [20] where the Poisson's ratio of polyacrylamide gels was measured to be 0.48-0.5. To further verify the incompressibility, we evaluate the determinant of the deformation gradient det(**F**) using our bead data. Note that $F_{ij} = \delta_{ij} + \partial u_i / \partial x_j$. Its determinant det(**F**) equals to the ratio of the deformed volume of a material element versus its undeformed volume. It turned out that det(**F**) ranges from 0.93 to 1.07 in most region, suggesting that the local volume change was within $\pm 7\%$. Given that the magnitude of strains can be up to 30% (see Fig.5), such a small local volume change confirms that the gel has a Poisson's ratio close to 0.5.

1.3.3. Experimentally obtained 3D stress field

Since the gel is nearly incompressible, directly calculating the stress fields using eq. (10) with a Poisson's ratio close to 0.5 can induce significant numerical errors. In this case, we need to compute the pressure and stress fields using eqns.(11) and (14-15). Recall that to determine the pressure field $p(\mathbf{x})$, eq. (14) requires a reference point $\mathbf{x}_0$ where the pressure is known. Ideally the reference point should be very far away from the deformation region such that all stress components vanish at this point. However, this is limited by the finite imaging volume of our experimental data, outside which there is no data points acquired for bead displacements. Therefore, we would not be able to compute the pressure field according to eq. (14) if the reference point were chosen outside the imaging volume. Here we choose the reference point to be on the top surface of the gel layer (z=0) and as far away from the contact center as possible. Specifically, the reference point is chosen to be $x_0=1.5h$, $y_0=0$, and $z_0=0$. At this point, the normal stress σ_{zz} should be zero since the surface is traction free. This condition, together with eq. (13), imply that $p(\mathbf{x}_0) = 2\mu\varepsilon_{zz}(\mathbf{x}_0)$. This result and the value of $\varepsilon_{zz}(\mathbf{x}_0)$ from the obtained strain field allow us to compute the pressure field using eq. (14) and then determine the stress field using eq. (13). The experimentally determined stress field is shown in Figure 1.6 for two normal stress components: σ_{xx}, σ_{zz} and a shear stress component σ_{xz}. Figure 1.6A and 1.6C suggest that the normal stresses are concentrated around the center of the contact region as expected, since this is the most severely deformed region within the gel.

Note that the stresses plotted in Figure 1.6 were normalized by the Young's modulus *E*, which can indeed be measured from our indentation data. Since the indenting force

is 12.4 μN, gel layer thickness h =134 μm, indenter radius R =585 μm (see section 2.2) and indentation depth δ=33.93μm (see section 2.7), taking the Poisson's ratio to be 0.5, the Young's modulus E is calculated to be 283 Pa using the formula in [29], and the shear modulus μ is 94 Pa.

1.3.4. Validation of the experimentally obtained 3D strain and stress field using finite element analysis

To validate the described 3D full field strain and stress mapping technique, we carried out an independent finite element analysis to determine the displacement, stress and strain fields within a thin polyacrylamide gel using the same setup as in our indentation experiments (Figure 1.1). The experimentally determined displacement fields (Figure 4A, 4C) and agree well with the FEM results (Figure 1.4B, 1.4D). Note that the contour levels in the experimental determined displacement fields were set to be the same as the FEM results, except for the maximum and minimum limits. Furthermore, the experimentally acquired strain fields (Figure 1.5A, 1.5C, 1.5E) agree well with those from FEM calculations (Figure 1.5B, 1.5D, 1.5F). This demonstrates the validity of the displacement measurements and the MLS interpolation method. The stress fields σ_{xx}, σ_{zz} and σ_{xz} from experiments are plotted and compared with FEM results both in contour plots and numerical plot (Figure 1.6A-G). Although the experimental results underestimate the magnitude of the normal stress components compared with FEM data, the distribution of stresses are still very well captured. Figure 1.6G plots the normalized stresses as functions of x/h on the contacting interface (z=0, y=0), further verifying our experimental techniques.

To highlight the impotance of the hydrostatic pressure field, we plot the stress component σ_{zz} as well as $2\mu\varepsilon_{zz}$ (both normalized by E) on the contacting interface in Fig.6H. Note that if the pressure term (or the $\lambda\varepsilon_b$ term in eq. (10)) were set to zero, the normal stress σ_{zz} would be equal to $2\mu\varepsilon_{zz}$. Fig. 6H clearly showed the significant deviation of $2\mu\varepsilon_{zz}$ from the stress σ_{zz} obtained from experimental or FEM results, thus demonstrating the necessity of accurately evaluating the pressure field. Furthermore, the excellent agreement between experimentally determined σ_{zz} and the FEM results validates our method of computing the pressure field.

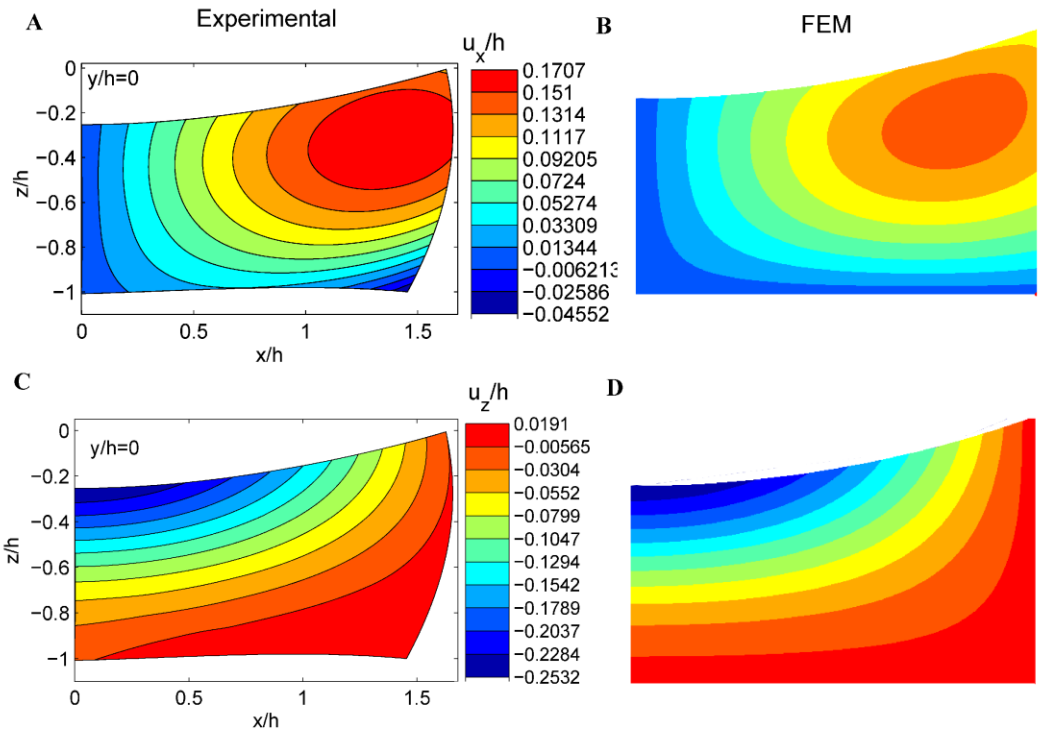

Figure 1.4 Continuous displacement fields from experiments and FEM calculations. Contour plots of the continuous displacement field u_x/h (A-B) and u_z/h (C-D) at the cross section y=0 and x>0. The same color map is used for experiments and FEM calculations.

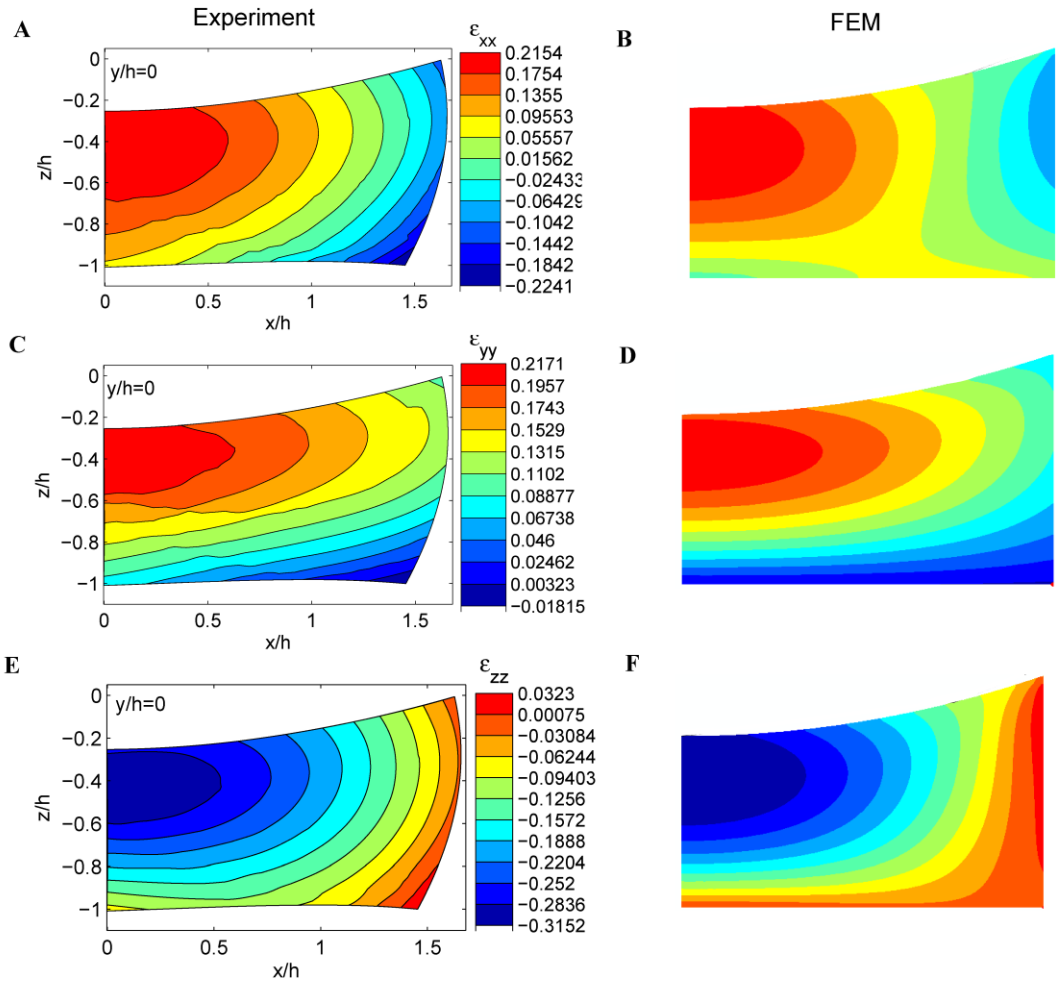

Figure 1.5 Strain fields from experiments and FEM calculations. Contour plots of strain field ε_{xx} (A-B), ε_{yy} (C-D) and ε_{zz} (E-F) at the cross section y=0 and x>0. The same color map is used for experiments and FEM calculations.

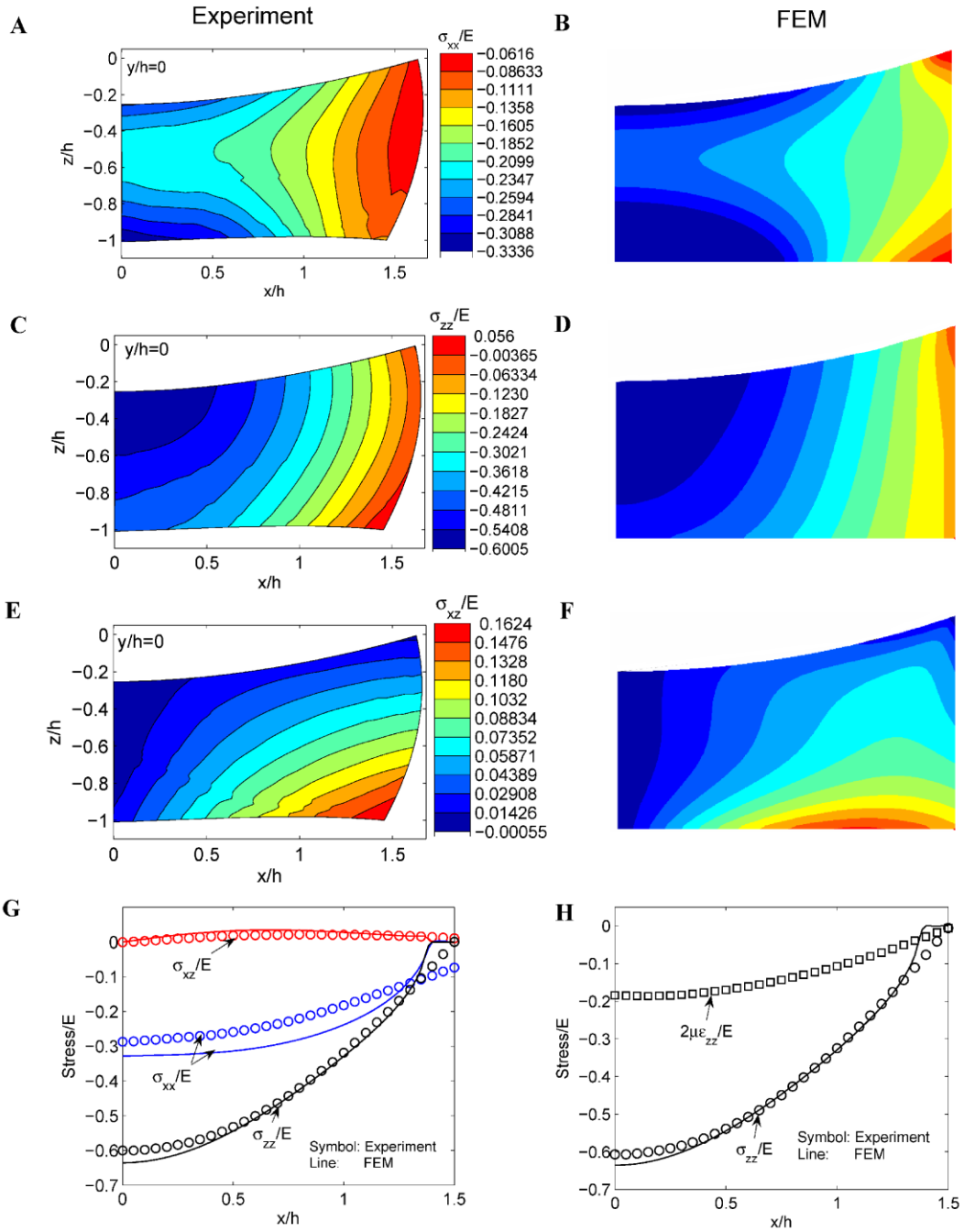

Figure 1.6 Stress field from experiments and FEM calculation. Contour plots of stress field σ_{xx}/E (A-B) σ_{zz}/E (C-D) and σ_{xz}/E (E-F) at the cross section y=0 and x>0. The same color map is used for experiments and FEM calculations. G: The normalized stresses versus x at the contact interface (y=0 and z=0). The symbols represent experimental results and the lines FEM results. H: The normalized normal stress σ_{zz}/E, and $2\mu\varepsilon_{zz}/E$ at the contact interface (y=0 and z=0). The symbols represent experimental results and the lines FEM results.

1.4. Conclusions and future perspectives

In summary, we have developed a 3D full field material characterization method for mapping the strain and stress field within a soft and transparent gel using a fluorescence microscope and a forward computation algorithm. This technique, together with a new method to compute the stress field in an incompressible elastic solid, allows us to map the strain and stress fields within a thin polyacrylamide gel when deformed by the weight of a millimeter scale glass sphere. The measured strain and stress field agree well with those obtained from the finite element method.

The use of the 3D defocused particle imaging method enables us to optimize the spatial and temporal resolutions needed for each application. Table 1.1 lists the spatial and temporal resolutions for the imaging system that we have (Microscope: IX 51, Olympus America Inc; Camera: DALSA 512B, EM, Waterloo, CA). For instance, to optimize the temporal resolution, we will take a single image for bead position measurements at a frame rate of 10fps. Under this scenario, the temporal resolution is 0.1sec, the fluorescent bead concentration expressed as average bead to bead spacing is 30 um for a 40X objective. To obtain a larger imaging volume, one can use a smaller magnification objective lens. In this case, a 20X objective lens will be able to increase the imaging volume by 8 times in comparison to a 40X lens. In addition, we can also take multiple images (10 in the table) along the z direction using an automatic z-translation stage to increase the imaging volume.

The main challenge is to reduce the spatial resolution for the bead displacement measurements. Currently, the average bead-to-bead spacing is 20- 30 um (Table 1.1) for the 3D defocused particle tracking method to work effectively. This limitation is

imposed by the ability to track overlapping rings when the beads are too close together. This problem can be resolved by (1)embedding fluorescent beads of different colors; (2) improving the tracking software. By embedding fluorescent beads of four different colors, once can reach a bead-to-bead spacing resolution of 12.5 um. The current tracking software only takes account the information of the ring diameter, however, the light intensity around the ring can also be used to identify the bead position.

Looking forward, the presented technique can be readily adapted to map the strain and stress field around a living cell embedded in a 3D ECM. The fast temporal resolution will allow us to probe cell traction force of cell types that change mechanically at a time scale that a confocal cannot handle, for example, cardiomyocytes. The use of a fluorescence microscope allows this technique to be more accessible to biology labs, in comparison to the current 3D traction microscopy where confocal microscopy is required. The introduction of a moving least squared method generates a straightforward, easy to implement method for mapping the 3D strain field in a soft gel using discrete bead displacements. More importantly, the forward computation algorithm (in comparison to solving an inverse problem using Green's function [22]) does not require that the biomaterials be linear nor deformation be small. Many commonly used natively derived biomaterials, such as collagen and fibrin, are known to exhibit nonlinear elastic behavior [27]. To extend the presented technique to nonlinear biological materials, one needs to simply modify the relation of stress and strain field using nonlinear elasticity theory. This work is currently in progress, and will be presented in a future publication.

Table 1.1 Spatial and temporal resolutions of the 3D traction microscopy.

Optimize For:	Spatial Resolution	Temporal Resolution	Image Volume
Magnification	40X (0.6 NA)	40X (0.6 NA)	20X (0.4 NA)
Number of Images	10	1	10
Total Image Volume [um^3]	205x205x150	205x205x40	410x410x300
Bead to Bead Spacing [um]	20	30	40
Acquisition Time [sec]	10	0.1	10
Single Bead Position Accuracy [um]	0.2x0.2x0.4	0.2x02x0.4	0.4x0.4x0.8

REFERENCES

1. Discher, D.E., P. Janmey, and Y.L. Wang, *Tissue cells feel and respond to the stiffness of their substrate.* Science, 2005. **310**(5751): p. 1139-1143.

2. Chen, C.S., *Mechanotransduction - a field pulling together?* Journal of Cell Science, 2008. **121**(20): p. 3285-3292.

3. Ulrich, T.A., E.M.D. Pardo, and S. Kumar, *The Mechanical Rigidity of the Extracellular Matrix Regulates the Structure, Motility, and Proliferation of Glioma Cells.* Cancer Research, 2009. **69**(10): p. 4167-4174.

4. Engler, A.J., et al., *Matrix elasticity directs stem cell lineage specification.* Cell, 2006. **126**(4): p. 677-89.

5. Isenberg, B.C., et al., *Vascular smooth muscle cell durotaxis depends on substrate stiffness gradient strength.* Biophys J, 2009. **97**(5): p. 1313-22.

6. Pelham, R.J., Jr. and Y. Wang, *Cell locomotion and focal adhesions are regulated by substrate flexibility.* Proc Natl Acad Sci U S A, 1997. **94**(25): p. 13661-5.

7. Peyton, S.R. and A.J. Putnam, *Extracellular matrix rigidity governs smooth muscle cell motility in a biphasic fashion.* Journal of Cellular Physiology, 2005. **204**(1): p. 198-209.

8. Tee, S.-Y., et al., *Cell Shape and Substrate Rigidity Both Regulate Cell Stiffness.* Biophysical Journal, 2011. **100**(5): p. L25-L27.

9. Engler, A., et al., *Substrate compliance versus ligand density in cell on gel responses.* Biophysical Journal, 2004. **86**(1): p. 617-628.

10. Griffith, L.G. and M.A. Swartz, *Capturing complex 3D tissue physiology in vitro.* Nat Rev Mol Cell Biol, 2006. **7**(3): p. 211-24.

11. Hebner, C., V.M. Weaver, and J. Debnath, *Modeling morphogenesis and oncogenesis in three-dimensional breast epithelial cultures.* Annual Review of Pathology-Mechanisms of Disease, 2008. **3**: p. 313-339.

12. Weaver, V.M., et al., *Reversion of the malignant phenotype of human breast cells in three-dimensional culture and in vivo by integrin blocking antibodies.* J Cell Biol, 1997. **137**(1): p. 231-45.

13. Levental, K.R., et al., *Matrix Crosslinking Forces Tumor Progression by Enhancing Integrin Signaling.* Cell, 2009. **139**(5): p. 891-906.

14. Cukierman, E., et al., *Taking cell-matrix adhesions to the third dimension.* Science, 2001. **294**(5547): p. 1708-1712.

15. Haessler, U., et al., *Dendritic cell chemotaxis in 3D under defined chemokine gradients reveals differential response to ligands CCL21 and CCL19.* Proc Natl Acad Sci U S A, 2011. **108**(14): p. 5614-9.

16. Wolf, K., et al., *Collagen-based cell migration models in vitro and in vivo.* Seminars in Cell & Developmental Biology, 2009. **20**(8): p. 931-941.

17. Dembo, M. and Y.L. Wang, *Stresses at the cell-to-substrate interface during locomotion of fibroblasts.* Biophysical Journal, 1999. **76**(4): p. 2307-2316.

18. Frey, M.T., et al., *Microscopic methods for measuring the elasticity of gel substrates for cell culture: Microspheres, microindenters, and atomic force microscopy.* Cell Mechanics, 2007. **83**: p. 47-65.

19. Schwarz, U.S., et al., *Calculation of forces at focal adhesions from elastic substrate data: The effect of localized force and the need for regularization.* Biophysical Journal, 2002. **83**(3): p. 1380-1394.

20. Maskarinec, S.A., et al., *Quantifying cellular traction forces in three dimensions.* Proceedings of the National Academy of Sciences of the United States of America, 2009. **106**(52): p. 22108-22113.

21. Hur, S.S., et al., *Live Cells Exert 3-Dimensional Traction Forces on Their Substrata.* Cellular and Molecular Bioengineering, 2009. **2**(3): p. 425-436.

22. Legant, W.R., et al., *Measurement of mechanical tractions exerted by cells in three-dimensional matrices.* Nature methods, 2010. **7**(12): p. 969-71.

23. Franck, C., et al., *Three-Dimensional Traction Force Microscopy: A New Tool for Quantifying Cell-Matrix Interactions.* Plos One, 2011. **6**(3).

24. Franck, C., et al., *Three-dimensional Full-field Measurements of Large Deformations in Soft Materials Using Confocal Microscopy and Digital Volume Correlation.* Experimental Mechanics, 2007. **47**(3): p. 427-438.

25. Wu, M., J.W. Roberts, and M. Buckley, *Three-dimensional fluorescent particle tracking at micron-scale using a single camera.* Experiments in Fluids, 2005. **38**(4): p. 461-465.

26. Belytschko, T., Y.Y. Lu, and L. Gu, *Element-Free Galerkin Methods.* International Journal for Numerical Methods in Engineering, 1994. **37**(2): p. 229-256.

27. Storm, C., et al., *Nonlinear elasticity in biological gels.* Nature, 2005. **435**(7039): p. 191-194.

28. Reinhart-King, C.A., M. Dembo, and D.A. Hammer, *Endothelial cell traction forces on RGD-derivatized polyacrylamide substrata.* Langmuir, 2003. **19**(5): p. 1573-1579.

29. Long, R., et al., *Effects of Gel Thickness on Microscopic Indentation Measurements of Gel Modulus.* Biophysical Journal, 2011. **101**(3): p. 643-650.

30. Lancaster, P. and K. Salkauskas, *Surfaces Generated by Moving Least-Squares Methods.* Mathematics of Computation, 1981. **37**(155): p. 141-158.

31. Mclain, D.H., *Drawing Contours from Arbitrary Data Points.* Computer Journal, 1974. **17**(4): p. 318-324.

32. Gordon, W.J. and J.A. Wixom, *Shepards Method of Metric Interpolation to Bivariate and Multivariate Interpolation.* Mathematics of Computation, 1978. **32**(141): p. 253-264.

33. Landau, L.D. and E.M. Lifshitz, *Theory of Elasticity*. 3rd ed1986: Butterworth-Heinemann.

34. Johnson, K.L., *Contact Mechanics*1987: Cambridge University Press.

35. Treloar, L.R.G., *THE ELASTICITY OF A NETWORK OF LONG-CHAIN MOLECULES .3.* Transactions of the Faraday Society, 1946. **42**(1-2): p. 83-94.

CHAPTER 2

3D CELL TRACTION MICROSCOPY

2.1 Introduction

Biomechanical interaction with the extracellular matrix (ECM) regulates the function of animal cells[1, 2]. The stiffness and adhesiveness of 2D substrates have been shown to affect cell growth[3], differentiation[4], migration[5-7], adhesive structures and dynamics[6], cytoskeleton assembly, and cell spreading[8, 9].

The 3D ECM *in vivo* provides both the biomechanical and biochemical cues that animal cells required to behave in a physiologically realistic manner[10-14]. As a result, an increasing number of *in vitro* models culture cells within the bulk of 3D hydrogels rather than on 2D substrates[10, 11, 15, 16]. However, efforts to understand and quantify cell generated forces are still dominated by cell traction microscopy on 2D substrates[17-19]. There is therefore a need to extend well established techniques for 2D traction microscopy into 3D.

An incremental step toward fully 3D traction microscopy was quantifying the entire 3D traction field of cells cultured on a compliant 2D substrate[20, 21]. Both Maskarinec et al. and Hur et al. mapped the cell generated 3D stress and strain fields within a polyacrylamide gel substrate by measuring fluorescent microsphere displacements with confocal microscopy. The displacements were then used as boundary conditions to solve the 3D governing equations of linear elasticity using finite element analysis.

Fully 3D traction microscopy of a cell embedded in hydrogel was demonstrated by Legant et al. who quantify cellular traction within a synthetic modified Polyethylene Glycol (PEG) elastic hydrogel[22]. Confocal microscopy was used to track cell induced displacements of fluorescent microspheres in the hydrogel and precisely record the cell surface. The cell surface was reconstructed and discretized into small

elements. The discretized Green's function of the cell surface elements was then obtained through finite element calculations. An ill posed inverse problem was then solved using an optimization method to determine cell traction from the fluorescent microsphere displacements. The method produces a high spatial resolution 3D traction field on the cell surface, but has inherent limitations. Due to the use of Green's function the method requires a linear elastic, isotropic, and homogenous hydrogel. Complex data acquisition and analysis are also required including solving thousands of finite element runs. Quantifying 3D traction of motile cells is also not possible because the PEG hydrogel has a high elastic modulus and a pore size much smaller than the cell.

We use a 3D traction microscopy method recently developed by Hall and Long et al. (chapter 1) to map the 3D stress field over time around an MDA-MB-231 malignant epithelial breast cancer cell migrating through an ECM (type I collagen)[23]. A fluorescence microscope is used to map the 3D displacement of fluorescent microspheres embedded in the ECM as opposed to the confocal microscope required by previous work. A simple easy to implement forward solution method is developed to calculate the 3D stress field from discrete microsphere displacements. The solution method is compatible with nonlinear materials such as type I collagen and other biologically derived hydrogels. Use of a low concentration collagen as the ECM allows for study of cell traction during migration through a 3D microenvironment[16].

2.2 Materials and methods

2.2.1 Cell culture

MDA-MB-231 (human epithelial malignant breast cancer) cells were cultured in low glucose Dulbecco's Modified Eagle Medium (DMEM) (Gibco Inc.) with 10% Fetal

Bovine Serum, 100 units/ml Penicillin, and 100 ug/ml Streptomycin. Cells were passed every 3 days and harvest for experiments in log phase 2-3 days after passage.

2.2.2 Well assay fabrication and surface treatment

A 6mm diameter Biopsy punch was used to punch wells in a 400um thick sheet of Polydimethylsiloxane (PDMS). The punched PDMS was oxygen plasma bonded to a 48x65mm no. 1 coverglass (Fisherbrand Inc.). A 10mm thick piece of Poly(methyl methacrylate) (PMMA) was sealed to the glass around the PDMS wells with high vacuum grease (Corning Inc.).

The PDMS wells were surface treated to covalently bond to collagen. The wells were coated with 1% Poly-ethylene-imine, incubated for 10 minutes, and then washed with distilled water. Next, the wells were coated with 0.1% glutaraldehyde and incubated for 30 minutes. The wells were then washed and incubated for 5 minutes with distilled water 4 times. The wells were then incubated overnight with distilled water, washed again in distilled water and aspirated before use.

2.2.3 Cell seeded collagen

Type I collagen was extracted from rat tails and suspended at a concentration of 5mg/ml in 0.1% acetic acid as described previously[24, 25]. The PDMS on glass well assay was also placed on ice along with three 1.5ml Eppendorf tubes. Components of the final collagen cell mixture were added to the three tubes and then combined to achieve the final cell embedded collagen. Here final concentration refers to the concentration in the final collagen cell mixture. In tube #1 10X Medium M199 and 1M NaOH were added for a final concentration of 1X and pH of 6.0. In tube #2 a suspension of MDA-MB-231 was diluted with DMEM media to achieve a final concentration of 25,000 cells/ml. 0.51um diameter green fluorescent carboxylated

polystyrene microspheres (Bangs Lab) were sonicated for 10 minutes then added to tube #2 to achieve an average bead to bead spacing of 10um in the final suspension. In tube #3 5mg/ml of collagen in 0.1M Acetic Acid was added to achieve a final collagen concentration of 2mg/ml. The contents of tube #2 were pipette into tube #1 and mixed by pipetting up and down. The contents of tube #1 were then pipette into tube #3 and pipetted up and down until mixing was complete. All tubes were kept on ice during the mixing process to slow collagen polymerization. A volume of collagen equal to the volume of each well was then pipetted into the PDMS well assay. The PDMS well assay was then incubated for 10 minutes on ice to slow polymerization and achieve more homogenous fibers. The assay was then incubated at 37C and 5% CO2 for 20 minutes. For the first 7.5 minutes the assay was incubated upside down and then flipped upside up for the remainder of the incubation to position the cells away from both the upper and lower gel boundaries. Low glucose DMEM media with 10% FBS and 100ng/ml Epidermal Growth Factor was pipetted on top of the polymerized cell seeded collagen gels. The cell seeded Collagen gels were then incubated at 37C and 5% CO2 overnight (12-16 hours) before imaging.

2.2.4 Time-lapse fluorescence microscopy

Imaging experiments were performed on a fluorescence microscope (Olympus IX-81) with an automated stage using a long working distance 40X magnification objective lens (Olympus LUCPlanFLN NA= 0.6). The software Metamorph (Olympus Inc.) was used for time-lapse imaging. The cells were kept at 37C and 5% CO2 throughout imaging.

10 cells were identified within the collagen gel that were both isolated from other cells and greater than 100um from any gel boundary. The location of each cell was recorded and a bright field image was captured for each cell. After 1 hour another

bright field image of the each cell was captured to determine migration direction. An initially cell-free volume of collagen directly in the path of each migrating cell was then imaged every 4 hours for 60 hours. At each time-point and location, a z-stack consisting of 165 images was taken in both bright field illumination mode for imaging the cell, and fluorescence mode for imaging the fluorescent microspheres. The total imaging volume was 217x165x151um (x,y,z) with a voxel size of 161x161x917nm. Total imaging time at a single cell position and time-point was about 9 minutes.

2.2.5Locating fluorescent microspheres and cell surface

The image stacks were first manually preprocessed to reduce stage drift and therefore improve tracking algorithm accuracy. The positions of the centroid of each of the fluorescent microspheres was then found using the commercial software Imaris (Bitplane Inc.). Imaris then used a proprietary autocorrelation algorithm to match and track the fluorescent microspheres over time. After the fluorescent microspheres were tracked across time, Imaris was used to apply a translational drift correction at each timepoint. The 3D cell surface and position were determined manually by identifying the area of the cell in focus at each z-stack level. The complete fluorescent microsphere and cell surface tracks were rendered in Imaris to visualize the displacement of the extracellular matrix by the cell (Figure 2.1).

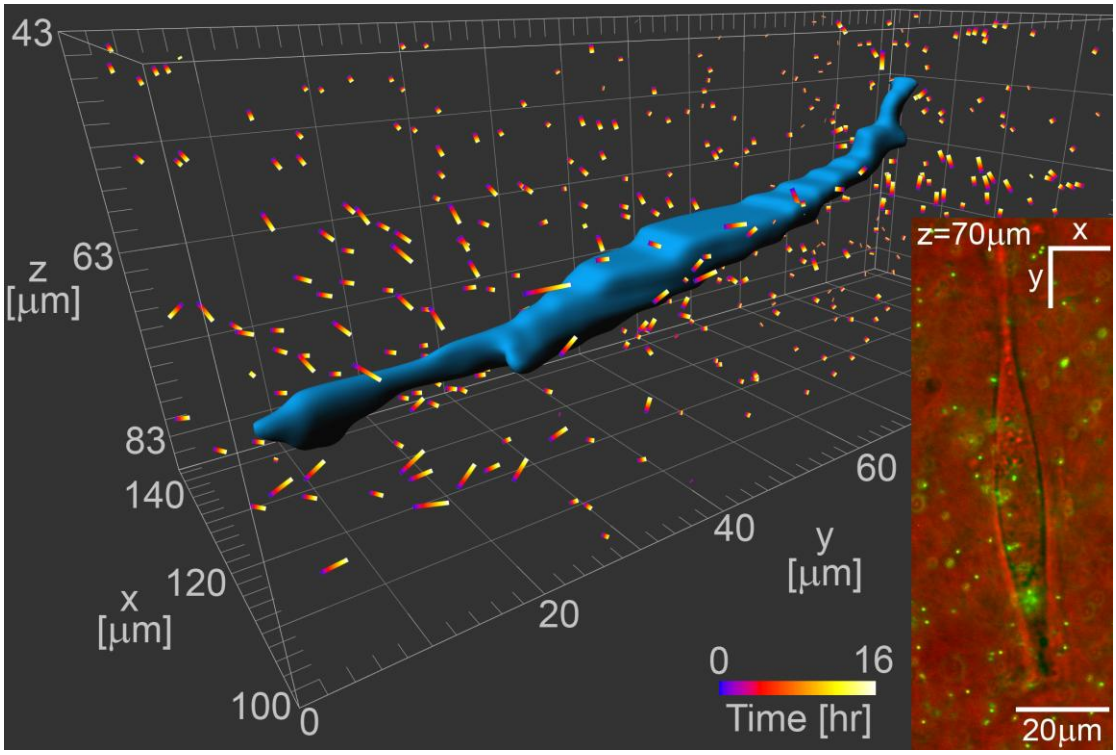

Figure 2.1. 3D discrete displacement field around a cell. The cell surface is rendered in blue. Each multicolor bar represent the measured fluorescent microsphere displacement over the course of 16 hours, where t=0 is defined as a time when the cell has not entered the viewing volume. Fluorescent microspheres are pulled toward either end of the cell. Inset is a composite bright field (red) and fluorescent (green) image of the plane at z=70um

2.2.6 Computing 3D stress field from the measured discrete displacements

The fluorescent microsphere displacements determined with Imaris are discrete measurements of the displacement field within the gel. A forward solution method previously developed and validated by Hall and Long et al (Chapter 1) was used to compute the 3D strain and stress fields from the discrete fluorescent bead displacements[23]. Briefly, the solution method begins by computing a continuous and differentiable displacement field from the discrete bead displacements using the Moving Least Squares Interpolation Method (MLSIM) (Figure 2.2)[26]. The continuous and differentiable displacement field allows for direct calculation of strain,

the spatial gradient of the displacement field. Knowing strain, stress can be calculated given a constitutive model for the 2.0 mg/ml collagen gel. For this work we assume that the collagen gel is linear elastic, so it can be defined by two parameters: Young's modulus and Poisson's ratio. We used a Young' modulus of 50 Pa[27] and a Poisson's ratio of 0.2 for 2.0 mg/ml Collagen gel. Knowing the 3D stress field of the collagen around the cell and the 3D cell surface from the bright field image stack, we can find the cell traction field which is the stress field at the cell surface.

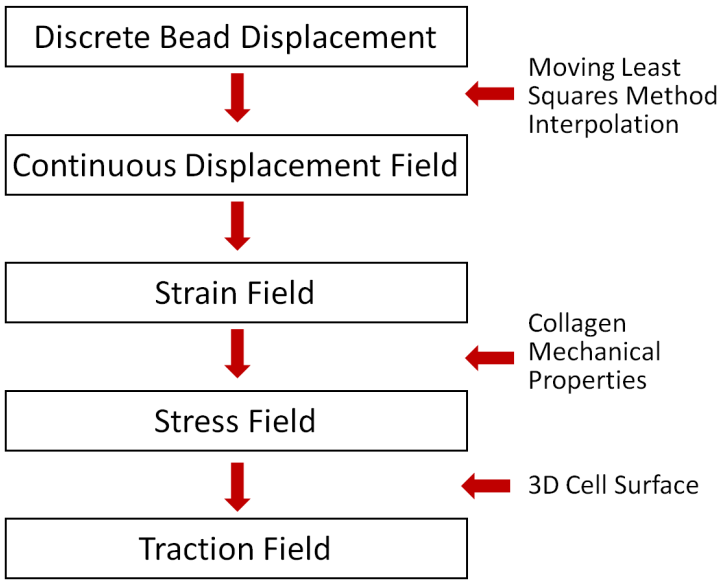

Figure 2.2. Flow chart of the forward computation algorithm for 3D traction microscopy.

2.3 Results and discussion

2.3.1 3D stress field

To better understand the stress field produced by the cell, the normal stress component σ_{cell} in the direction of the cell's polarization was plotted in a 3D volume around the cell (Figure 2.3). σ_{cell} is in strong compression near the cell which is expected as the reference configuration is an empty collagen volume. When the cell is added to the

volume its volume must displace collagen fibers creating a compressive stress field near the cell. There is a region of strong tension directly in front of the cell in the direction of migration. We expect the cell to be in tension along the direction of its polarization as it must contract to pull its mass forward. Tension in the ECM localized to the front of the cell is therefore in line with expectation for a migrating cell.

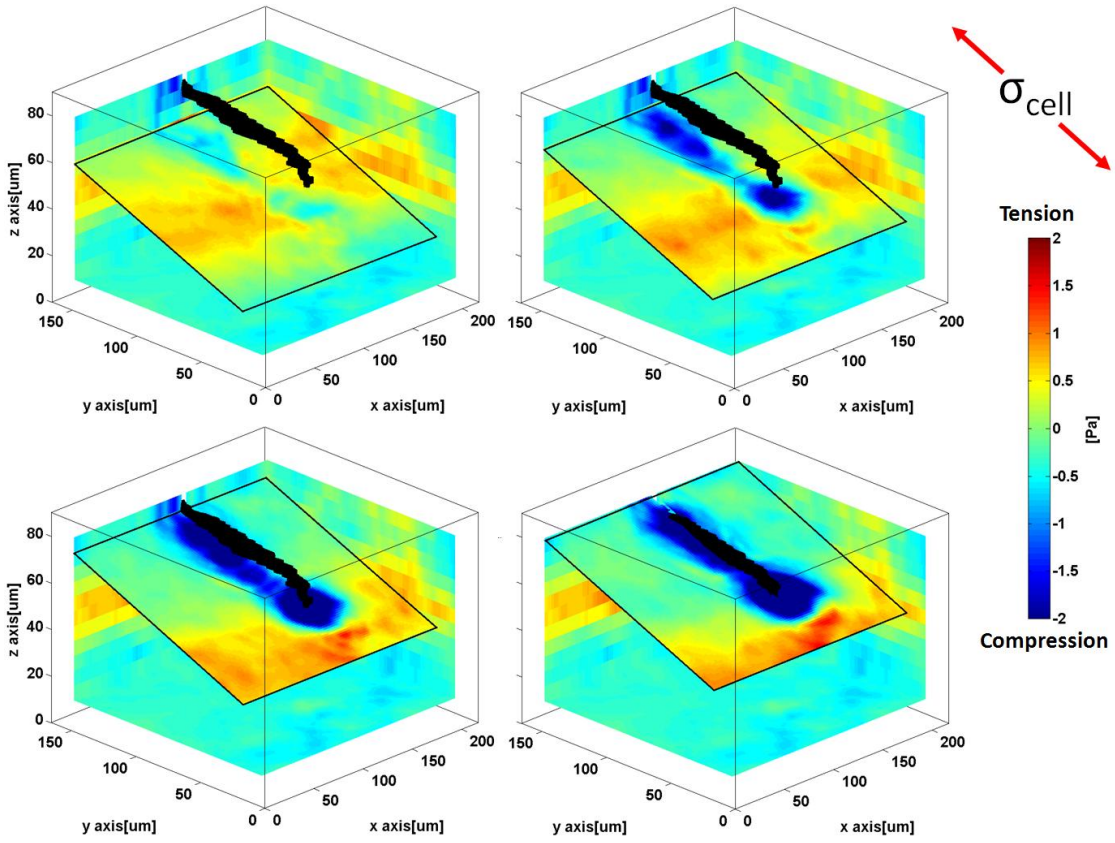

Figure 2.3. 3D Stress field around the cell. The normal stress component in the direction of the cell's polarization σ_{cell} is rendered on 4 planes around the cell (black) at time t=16 hours.

2.3.2 Stress field over time

The normal stress field σ_{yy} is plotted over time as a cell migrates into an initially void volume of collagen over the course of 16 hours (Figure 2.4A). The time resolution of 4 hours is insufficient to clearly resolve any cyclic loading of the extracellular matrix that may be present. However, the stress fields shift in space over time as the cell migrates and supports known mechanisms for cell motility. At t=8 hours the cell has projected a series of filopodia into the volume causing high compression in σ_{yy} as the filopodia are pushed into the collagen matrix by actin filament polymerization. At t=12 hours the cell has moved mostly into the cell volume and an area of tension is apparent in front of the cell. At t=16 hours the cell is in approximately the same position but has moved a large amount of its mass toward the front of the cell and there is a strong area of tension in front of the cell suggesting myosin II driven contraction on the cytoskeleton along the length of the cell's polarization.

σ_{xy} is plotted over time in the same manner as σ_{yy} to see if other stress components can also shed light on the cell's behavior (Figure 2.4B). We observe an opposite sign for σ_{xy} in the extracellular matrix on either side of the front end of the migrating cell. To understand this stress field in terms of cell behavior, first note that the cell is migrating downward and in a strong state of tension at its front end at t=16 hours so we expect the front of the cell to pull up on the extracellular matrix. A stress element located in the extracellular matrix on the left side and toward the front of the cell will experience an upward shear on its right face which is positive by our sign convention. Conversely, a stress element located on the right side of the cell will experience an upward shear on its left face corresponding to negative shear as observed in our data. At the back of the cell at t=16 hours the cell is pulling down in the direction of migration as opposed to up at the front thus reversing the sign of σ_{xy} from the front of the cell.

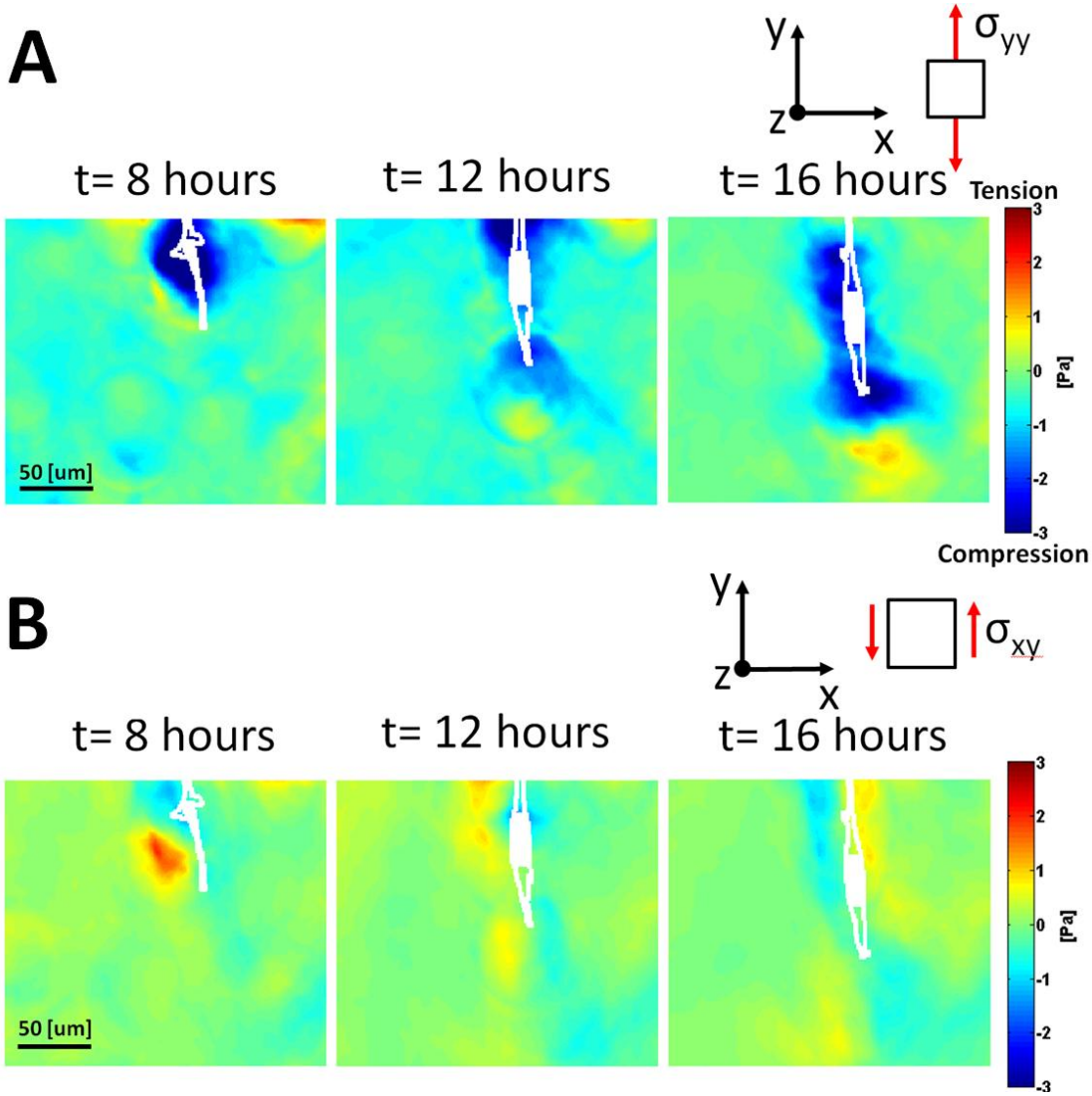

Figure 2.4. Normal and shear stress fields over time. The 3D stress field in the ECM is rendered on a plane near the center of the cell for both σ_{yy} (A) and σ_{xy} (B) at times t=8, 12, and 16 hours from the reference configuration. An outline of the cell projected onto the rendering plane is drawn over the image in white. The area of the cell lying in the rendering plane is shaded in white.

2.4 Conclusions and future perspectives

In summary, we have mapped the 3D stress field in collagen around a migrating MDA-MB-231 epithelial breast cancer cell over time. Both normal and shear components of the stress field were useful in understanding the behavior of the cell in terms of molecular and cell scale mechanical processes. Only the fluorescence microscope common in cell biology laboratories was required to record the 3D displacement of the ECM around the cell.

Use of fluorescence microscopy allows for high throughput low cost experiments. As demonstrated, multiple cell positions can be imaged over time in parallel using a fluorescence microscope with an automated stage. Time resolution for a single imaging location is limited by cell phototoxicity rather than acquisition rate. We found that cells experience phototoxic effects if the time-step was reduced below 1 hour on our imaging system for the z-stack size used in this work. Improved resolution and reduced cell phototoxicity are possible using a fluorescence microscope by using a high numerical aperture water or Silicone immersion lens in place of the long working distance lens used in this work. Confocal microscopy is also completely compatible with our method for applications that require even higher resolution.

Further characterization of the type I collagen may be required to accurately translate measured strain fields to stress fields. We observed a maximum strain of 15% while Storm et al. observed nonlinearity using a shear strain-controlled rheometer at shear strain above 0.01 for 2mg/ml collagen[27]. Another potential complication is that average pore size of the 2mg/ml collagen gel on the order of 10um is comparable in size to the cell width. With such a large pore size there may be significant error in assuming a continuum material model. Increasing the concentration of the collagen gel will reduce the pore size, but it will also reduce cell motility. The collagen gel concentration must therefore be carefully tuned to allow for both cell motility and use

of a continuum material model. This constraint prevents studies of differential cell behavior during migration at different collagen concentrations. However, study of differential cell behavior at varying gel stiffnesses can still be achieved by glycating the collagen gel with Ribose[28]. Because Ribose acts as a crosslinker, a large enough pore size to facilitate cell motility through the collagen gel can be maintained at higher gel stiffnesses. The crosslinking of the glycated gel may also lead to more linear elastic material behavior over a larger strain regime eliminating the requirement for precise characterization of the nonlinear properties of low concentration type I collagen gels. While cells pull with greater force on stiffer ECM's, we expect ECM displacement to decrease with increasing stiffness. The usable ECM stiffness range is therefore limited by ability to resolve displacement of the fluorescent microspheres embedded in the ECM. Higher resolution imaging techniques like confocal microscopy would thus allow study of 3D cell traction at higher ECM stiffness.

In the future, the 3D cell traction microscopy method can be used to answer questions in cell biology and cancer metastasis. Mesenchymal and amoeboid models for cell motility are currently posited to cells migrating in 3D environments. Study of the 3D traction of MDA-MB-231 cells of varying polarization could shed light on the accuracy of these models. Reducing the time resolution from 4 hours to 1 hour may allow quantification of any cyclic loading of the 3D ECM as the cell migrates. A potential correlation between 3D traction and cancer cell malignancy could be studied by comparing the traction of a highly malignant cell line such as MDA-MB-231 to a less malignant line like MCF-7.

Beyond cell migration through a bulk ECM, the mechanics of cell intravasation and extravasation central to cancer metastasis could be studied with a carefully designed transmigration microfluidic assay (Figure 2.5). Using contact line pining, cell seeded collagen can be confined to the left and right side of a central channel[29]. Epithelial

cells could then be flowed through the center channel to form a monolayer as an analog to the basal membrane of a blood or lymphatic vessel. Flow in the outside channels and central channel of the device can be used to control the chemical environment and produce concentration gradients of chemoattractant and chemorepellants. The same device could also be configured to record the mechanics of a very high concentration of cells as an analog to a tumor. Our 3D traction microscopy method can thus be adapted to experiments for studying cell mechanics across the entire process of cancer metastasis including mechanics around a tumor, migration of a single cell through a bulk ECM, and intravasation and extravasation at a blood or lymph vessel.

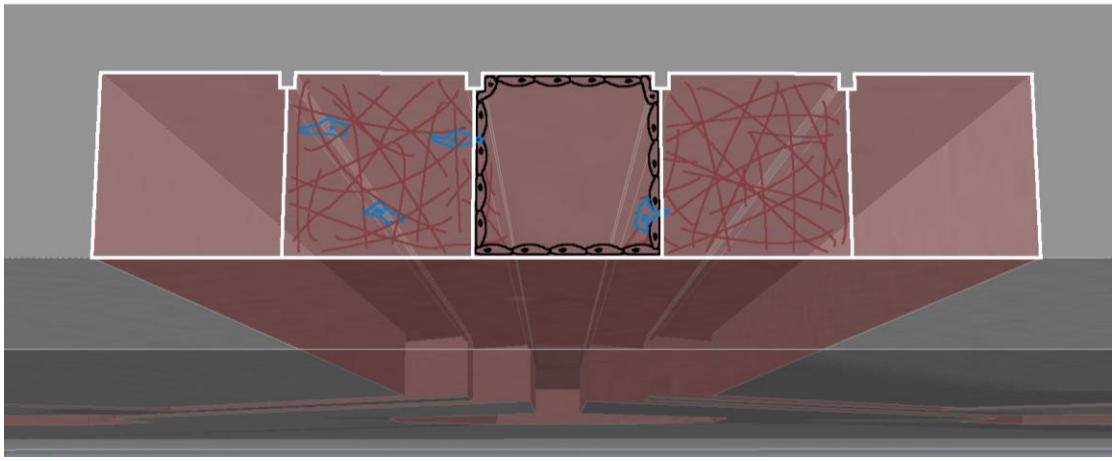

Figure 2.5. Transmigration microfluidic device for 3D traction microscopy. Type 1 collagen (brown lines) is confined to two channels around a center channel through contact line pinning. Epithelial cells (black) are flowed through the center channel to form a monolayer. Chemical concentration gradients are established through flow in the side and middle channel. 3D traction of cancer cells (blue) can be studied during intravasation and extravasation from the center channel.

REFERENCES

1. Discher, D.E., P. Janmey, and Y.L. Wang, *Tissue cells feel and respond to the stiffness of their substrate.* Science, 2005. **310**(5751): p. 1139-1143.

2. Chen, C.S., *Mechanotransduction - a field pulling together?* Journal of Cell Science, 2008. **121**(20): p. 3285-3292.

3. Ulrich, T.A., E.M.D. Pardo, and S. Kumar, *The Mechanical Rigidity of the Extracellular Matrix Regulates the Structure, Motility, and Proliferation of Glioma Cells.* Cancer Research, 2009. **69**(10): p. 4167-4174.

4. Engler, A.J., et al., *Matrix elasticity directs stem cell lineage specification.* Cell, 2006. **126**(4): p. 677-89.

5. Isenberg, B.C., et al., *Vascular smooth muscle cell durotaxis depends on substrate stiffness gradient strength.* Biophys J, 2009. **97**(5): p. 1313-22.

6. Pelham, R.J., Jr. and Y. Wang, *Cell locomotion and focal adhesions are regulated by substrate flexibility.* Proc Natl Acad Sci U S A, 1997. **94**(25): p. 13661-5.

7. Peyton, S.R. and A.J. Putnam, *Extracellular matrix rigidity governs smooth muscle cell motility in a biphasic fashion.* Journal of Cellular Physiology, 2005. **204**(1): p. 198-209.

8. Tee, S.-Y., et al., *Cell Shape and Substrate Rigidity Both Regulate Cell Stiffness.* Biophysical Journal, 2011. **100**(5): p. L25-L27.

9. Engler, A., et al., *Substrate compliance versus ligand density in cell on gel responses.* Biophysical Journal, 2004. **86**(1): p. 617-628.

10. Griffith, L.G. and M.A. Swartz, *Capturing complex 3D tissue physiology in vitro.* Nat Rev Mol Cell Biol, 2006. **7**(3): p. 211-24.

11. Hebner, C., V.M. Weaver, and J. Debnath, *Modeling morphogenesis and oncogenesis in three-dimensional breast epithelial cultures.* Annual Review of Pathology-Mechanisms of Disease, 2008. **3**: p. 313-339.

12. Weaver, V.M., et al., *Reversion of the malignant phenotype of human breast cells in three-dimensional culture and in vivo by integrin blocking antibodies.* J Cell Biol, 1997. **137**(1): p. 231-45.

13. Levental, K.R., et al., *Matrix Crosslinking Forces Tumor Progression by Enhancing Integrin Signaling.* Cell, 2009. **139**(5): p. 891-906.

14. Cukierman, E., et al., *Taking cell-matrix adhesions to the third dimension.* Science, 2001. **294**(5547): p. 1708-1712.

15. Haessler, U., et al., *Dendritic cell chemotaxis in 3D under defined chemokine gradients reveals differential response to ligands CCL21 and CCL19.* Proc Natl Acad Sci U S A, 2011. **108**(14): p. 5614-9.

16. Wolf, K., et al., *Collagen-based cell migration models in vitro and in vivo.* Seminars in Cell & Developmental Biology, 2009. **20**(8): p. 931-941.

17. Dembo, M. and Y.L. Wang, *Stresses at the cell-to-substrate interface during locomotion of fibroblasts.* Biophysical Journal, 1999. **76**(4): p. 2307-2316.

18. Reinhart-King, C.A., M. Dembo, and D.A. Hammer, *Endothelial cell traction forces on RGD-derivatized polyacrylamide substrata.* Langmuir, 2003. **19**(5): p. 1573-1579.

19. Jannatt, R.A., M. Dembo, and D.A. Hammer, *Traction Forces of Neutrophils Migrating on Compliant Substrates.* Biophysical Journal, 2011. **101**(3): p. 575-584.

20. Maskarinec, S.A., et al., *Quantifying cellular traction forces in three dimensions.* Proceedings of the National Academy of Sciences of the United States of America, 2009. **106**(52): p. 22108-22113.

21. Hur, S.S., et al., *Live Cells Exert 3-Dimensional Traction Forces on Their Substrata.* Cellular and Molecular Bioengineering, 2009. **2**(3): p. 425-436.

22. Legant, W.R., et al., *Measurement of mechanical tractions exerted by cells in three-dimensional matrices.* Nature methods, 2010. **7**(12): p. 969-71.

23. Hall, M.S., et al., *Mapping Three-Dimensional Stress and Strain Fields within a Soft Hydrogel Using a Fluorescence Microscope.* Biophysical Journal, 2012.

24. Bornstein, M.B., *Reconstituted Rat-Tail Collagen Used as Substrate for Tissue Cultures on Coverslips in Maximow Slides and Roller Tubes.* Laboratory Investigation, 1958. **7**(2): p. 134-137.

25. Cross, V.L., et al., *Dense type I collagen matrices that support cellular remodeling and microfabrication for studies of tumor angiogenesis and vasculogenesis in vitro.* Biomaterials, 2010. **31**(33): p. 8596-8607.

26. Belytschko, T., Y.Y. Lu, and L. Gu, *Element-Free Galerkin Methods.* International Journal for Numerical Methods in Engineering, 1994. **37**(2): p. 229-256.

27. Storm, C., et al., *Nonlinear elasticity in biological gels.* Nature, 2005. **435**(7039): p. 191-194.

28. Roy, R., A. Boskey, and L.J. Bonassar, *Processing of type I collagen gels using nonenzymatic glycation.* Journal of Biomedical Materials Research Part A, 2010. **93A**(3): p. 843-851.

29. Kalinin, Y.V., V. Berejnov, and R.E. Thorne, *Contact Line Pinning by Microfabricated Patterns: Effects of Microscale Topography.* Langmuir, 2009. **25**(9): p. 5391-5397.